Journal of Power Sources 185 (2008) 1524–1532

Contents lists available at ScienceDirect

Journal of Power Sources

journal homepage: www.elsevier.com/locate/jpowsour

A fully integrated microbattery for an implantable microelectromechanical system

F. Albano[a,d], Y.S. Lin[b], D. Blaauw[b], D.M. Sylvester[b], K.D. Wise[b,c], A.M. Sastry[a,c,d,*]

[a] Department of Material Science Engineering, University of Michigan, Ann Arbor, MI 48109, United States
[b] Department of Electrical Engineering and Computer Science, University of Michigan, Ann Arbor, MI 48109, United States
[c] Department of Biomedical Engineering, University of Michigan, Ann Arbor, MI 48109, United States
[d] Department of Mechanical Engineering, University of Michigan, Ann Arbor, MI 48109, United States

ARTICLE INFO

Article history:
Received 9 July 2008
Received in revised form 16 August 2008
Accepted 20 August 2008
Available online 29 August 2008

Keywords:
Microbattery
Integrated
MEMS
POWER
Thin-film
PVD
Implantable

ABSTRACT

The Wireless Integrated Microsystems Engineering Research Center's Intraocular Sensor (WIMS-ERC IOS) was studied as a model system for an integrated, autonomous implantable device. In the present study, we had four objectives: (1) select and designing an optimized power supply for the WIMS-IOS; (2) develop a fabrication technique allowing small scale, low-cost, and integrable fabrication for CMOS systems, and experimentally demonstrate a microscopic power source; (3) map capacity and lifetime of several fabricated microbatteries; (4) determine the effects of miniaturization on capacity, lifetime and device architecture.

Physical vapor deposition (PVD) was used to deposit thin layers ($\leq$1 μm) of metal sequentially onto glass substrates (SiO_2, as used in the device). To map the influence of size over cell capacity and cycle life, we fabricated and tested five stand-alone cells using a Solartron® 1470E battery tester and a Maccor® 4000 series tester. A sixth battery was fabricated to investigate the effects of system integration, variable discharge rate and size reduction simultaneously. The highest experimental capacity among the larger cells O(cm^2) was 100 μAh, achieved by IOS-C-1 at 250 μA (1.4 C) discharge. Among O(mm^2) cells, IOS-M-1 achieved the highest capacity (2.75 μAh, ~76% of theoretical) at 2.5 μA discharge (0.7 C rate).

1. Introduction

The reduction in size and improvement in capability of microsystems is presently limited by the specific and gravimetric properties, and overall sizes, of on-board power supplies [1]. This is most readily seen in autonomous devices used in environmental [2] biological [1,3] and medical [4–6] applications (Table 1), which rely mainly on batteries for power. Indeed, power supplies often comprise up to ten times the mass of the other elements of the system, combined.

The Wireless Integrated Microsystems Engineering Research Center's Intraocular Sensor (WIMS-ERC IOS) was studied here as a model system for an integrated, autonomous implantable device. This device is based on the Phoenix Processor [7,8], an ultra low power consumption platform (~30 pW) used in several WIMS microsystems. Its small scale (~0.4 mm^3 in volume, with a footprint of ~2 mm^2, Fig. 1) is required, to allow implantation in the eye to monitor intraocular pressure during treatment of glaucoma, for up to 2 years. At present (Table 2), there is no commercial power supply available which fits within the 2 mm^2 device area, and simultaneously meets the lifetime and implantability requirements of the device.

Despite their excellent volumetric energy (Table 2), existing thin-film batteries require surface areas of O(cm^2) to power typical MEMS devices, for more than 1 day. With specific capacities of 100–300 μAh cm^{-2}, limited by the maximum thickness of thin-film electrodes construction (<5 μm), these batteries have been unable to meet the required lifetime of MEMS sensors and actuators. Moreover, typical thin-film processing conditions involve high temperatures (500–900 °C) and masking and etchant materials that are incompatible with chip materials and packages. To date, none has been implemented or integrated as power supply in a MEMS of the scale described here; instead, novel devices of similar scale have been demonstrated using macroscopic, unintegrated power sources (Table 1).

* Corresponding author at: Department of Mechanical Engineering, University of Michigan, Ann Arbor, MI 48109, United States. Tel.: +1 7346475926; fax: +1 7346479379.
E-mail address: amsastry@umich.edu (A.M. Sastry).

0378-7753/$ – see front matter © 2008 Elsevier B.V. All rights reserved.
doi:10.1016/j.jpowsour.2008.08.061

Nomenclature

C	discharge rate (A); C/5 is the current (A) to fully discharge a battery in 5 h
CI	cochlear implant
CVD	chemical vapor deposition
DC	duty cycle
E^0	standard electrode potential (V)
FEG	field emission gun
IOS	intraocular sensor
IOS-C-1	first O(cm^2) battery prototype
IOS-C-2	second O(cm^2) battery prototype
IOS-C-3	third O(cm^2) battery prototype
IOS-M-1	first O(mm^2) battery prototype
IOS-M-2	second O(mm^2) battery prototype
IOS-X-1	on-chip battery prototype
MAV	micro-air vehicle
MEMS	microelectromechanical system
O()	Landau notation, O(cm^2) = order of cm^2
POWER	power optimization for wireless energy requirements, a Matlab® algorithm
PVD	physical vapor deposition
SEM	scanning electron microscope
SOA	state of the art
WIMS-ERC	Wireless Integrated Microsystems-Engineering Research Center
XEDS	X-ray energy dispersive spectroscopy

Possibly the most significant development in autonomous MEMS in the coming decades, for new applications, will be the achievement of fully integrated and optimized power supplies, realized cost-effectively, that are also capable to achieve energy densities (~27 mWh cm^{-2} [9]) required to operate MEMS. Adopting manufacturing techniques that can be performed outside the clean room [10], which are also compatible with CMOS fabrication techniques, have the potential to reduce processing steps. Thus, in the present study, we had four objectives:

(1) Select and designing an optimized power supply for the WIMS-IOS;
(2) develop a fabrication technique allowing small scale, low-cost, and integrable fabrication for CMOS systems, and experimentally demonstrate a microscopic power source;
(3) map capacity and lifetime of several fabricated microbatteries;

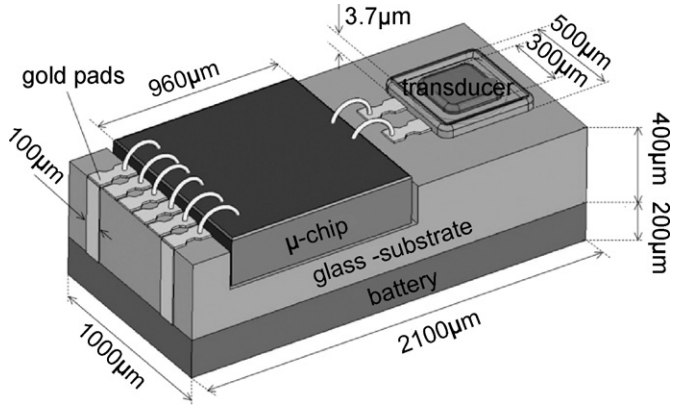

Fig. 1. WIMS-ERC IOS with integrated battery [38].

Table 1
Survey of battery powered MEMS [1–6]

Microsystem	Application	System volume (no battery) (mm^3)	Battery volume (mm^3)	System mass (no battery) (g)	Battery mass (g)	Battery chemistry	Clinical test	Year	Refs.
Cyborg beetle	Micro-air vehicle (MAV)	3.0 (no electrodes)	110	0.26	0.4	Zn–air	Green June Beetle (*Cotinis Texana*)	2008	[1]
Multi-sensor	Environmental/biological monitoring	150	350	0.25	3.0	Lithium	n/r	2006	[2]
Bio-potential recording system	Biological potential monitoring	7.3×10^{-3}	326	1.1 (with battery)	n/r	n/r (1.5 V)	Marmoset monkey (*Callithrix Jacchus*)	2005	[3]
Microelectronic pill	Remote biomedical measurements	0.5	1.2×10^3	7.0	5.2	Zn/AgO	n/r	2004	[4]
Neural recording system	Neural recording	3.51×10^5	1.61×10^5	195	40	Li-ion	Rhesus macaque (*Maccaca mulatta*) owl monkey (*Aotus nancymae*)	2004	[5]
Radio-transmitter	Neural recording	1.25×10^3	800	3.1	1.0	Zn–air	Behaving barn owls (*Tyto alba*)	2000	[6]

Table 2
Survey of microbatteries [10,23–31,39–46]

	Year								
	1995	1999–2000	1999–2000	1996–1999	1996–1999	2004	2007	2001	2007
Process	Sputtering, thermal evaporation			Pulsed laser deposition			LPCVD, sputtering etching	Sputtering, electroplating	PVD
Cathode	V_2O_5	$LiCoO_2$	Mn_2O_4	$LiCoO_2$	$LiMn_2O_4$	$LiNi_{0.8}Co_{0.15}Al_{0.05}O_2$	Pt	NiOOH	AgO
Anode	Li	Li	Li	Li	Li	Cu_2Sb	Al	Zn	Zn
Electrolyte	LIPON	LIPON	Solid Li glass	$LiCLO_4$	$LiCLO_4$	EC/DEC	KOH/KCl/H_2O_2	20 wt% KOH–ZnO	27 wt% KOH
Nominal voltage (V)	3.75	4.0	4.0–4.5	3.2–3.6	3.2–3.6	2.4–4	0.8–1.3	1.7–1.8	1.55
Thickness (μm)	7–15	2.2*–15	0.3*	0.2–1.5*	0.2–1.5*	0.25	6	100	25
Area (cm^2)	1.21	1.0*–3.22	1.0*	3.0	3.0	1.0	1.0	0.007*–0.02	1.0
Capacity (μAh)	13.5–18.5	160	15	216	252	300	64	1.9–6.79	100
Discharge current (μA)	2.42–48.4	100	10	30	30	40	240	n/r	250
$\tilde{c}$ (μAh cm^{-2})	20–120	60–150	20–60	72	84	300	400	277–970	100
$\hat{i}$ (μA cm^{-2})	2–40	100–4000	n/r	10	10	40	240	7–10^5	250
$\hat{p}$ (mW cm^{-2})	n/r	30	30	n/r	n/r	n/r	4.8–6.5	70	0.4
$\tilde{e}$ ($Wh\,l^{-1}$)	425	2070	n/r	n/r	n/r	n/r	300–600	55	40
$\tilde{e}$ (Wh kg^{-1})	101	n/r	n/r	n/r	n/r	n/r	n/r	n/r	3.0
Refs.	[1]	[2–6]	[2–6]	[7–9]	[7–9]	[10]	[11]	[12–14]	[16]

* Thickness of the cathode only.

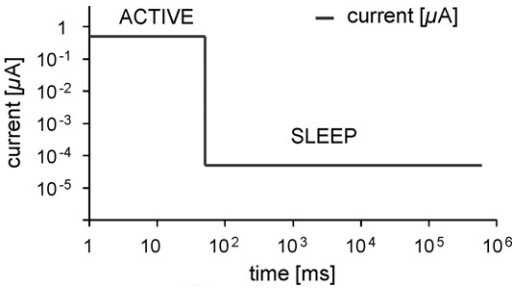

Fig. 2. WIMS-ERC IOS microchip duty cycle.

(4) determine the effects of miniaturization on capacity, lifetime and device architecture.

Our methodology builds on our prior efforts in the area, including optimization of power supplies [11,12], manufacture of novel microbatteries [13,10] and electrode optimization [14,15].

2. Methods

2.1. Testbed

The WIMS-ERC intraocular sensor has a bimodal duty cycle (Fig. 2) comprising ~10 min periods of "sleep," punctuated by 30–50 ms (milliseconds) periods of "active" sensing (Fig. 2). A 1-month duty cycle was assumed; a constant voltage step of 1.5 V at a constant current draw of 100 nA during 1 h, repeated 720 times was used. Voltage regulation in the chip was necessitated by operation and control, at different voltages, of several components; it was accomplished (Fig. 4) by use of a DC/DC converter capable of converting variable voltages ranging 1.0–1.6 V down to constant voltages of 0.1–0.4 V. The geometric constraints were a surface area of 3 mm^2 (i.e. the entire area above the chip surface or up to the entire area on the back of the device substrate) and a volume of ~0.42 mm^3 (Fig. 1).

2.2. Battery design

We evaluated implementation of available commercial systems, using a previously built algorithm, POWER [11,12]. This algorithm evaluates three different optimization approaches to screen a user-defined commercial database of cells and to identify candidate cells. In our selection approaches, we included considerations of energy and power densities, coupled with models for losses in capacity over time and over cycling (secondary cells) of the cells. Electrochemistries considered included primary silver oxide (Zn/AgO, Table 3), alkaline, zinc and lithium batteries (totaling 194 cells [11]) and secondary Li-ion, Nickel (NiMH and Ni–Zn) and lithium polymer batteries (totaling 61 cells [11]), covering a wide range of commercially available chemistries and several thin-film research systems.

2.3. Battery fabrication

Physical vapor deposition (PVD) was used to deposit thin layers (≤1 μm) of titanium (Ti, adhesion layer), gold (Au, current collector) and silver (Ag, active material) sequentially onto glass substrates (SiO_2, same as the device). A vacuum chamber type EvoVac® A-Mod from Ångstrom Engineering [16] with a pressure of the order of 10^{-7} Torr was employed; pure metal particles of few millimeter diameters were melted and evaporated into gas phase from resistively heated boats at the bottom of the chamber. The substrate

Table 3
POWER Zn/AgO database used for analysis [47,48]

Electrochemistry	Manufacturer	Number of cells included	Accounting for capacity fade	Specific energy ($Wh\,kg^{-1}$)	Energy density ($Wh\,l^{-1}$)	Specific power ($W\,kg^{-1}$)		Power density ($W\,l^{-1}$)
						Calculated [1]	Literature	
Zn–AgO	Renata	42	8	62–128	253–516	0.1–0.2	600 [2]	0.3–0.8
	Duracell	14	1	73–120	270–500	0.01–1		0.4–4
	Maxell	43	2	2–116	75–600	0.002–0.25		0.06–1
	Energizer	43	1	50–150	200–500	0.1–1		0.4–4

was attached to a rotating disk (constant speed, to provide uniform deposition) at the top of the chamber. Films were deposited using a maskless approach. Deposition rates and thickness of the films were monitored through multiple mass sensors located inside the chamber, and controlled through the instrument software. After PVD was completed, the films were removed from the chamber and oxidized in ozone (O_3) atmosphere, using a UVO Cleaner® 342 machine for 10 and 15 min.

Anodes were deposited by directly spraying zinc (Zn) nanopowder, obtained from 3 M [17], on top of copper foil (Cu) current collectors at room temperature and atmosphere. A Celgard® 3401 microporous membrane (25 μm thick) was used as separator and hold in place by two silicone gaskets utilized to seal the battery. The hermetic seal was achieved by means of the gaskets and a set of Plexiglass clamps. An aqueous solution of potassium hydroxide (28% KOH, 1% Li, from Yardney Technical Products Inc.) was employed as electrolyte. The reaction chamber between the anode and cathode was completely filled with the electrolyte before clamping. In Table 4 we report the final footprint and cathode mass of the battery prototypes after assembly.

2.4. Materials imaging

Morphologies and microstructures of the anode and cathode films were imaged in a Philips XL30 FEG scanning electron microscope (SEM), before battery prototypes were assembled. Anode porosity and particles sizes were recorded. Uniformity of the cathode films was qualitatively estimated by analyzing the surface images. X-ray energy dispersive spectroscopy (XEDS) capabilities of the instrument were utilized to verify the purity of the deposited samples and to detect the elemental composition of the electrodes.

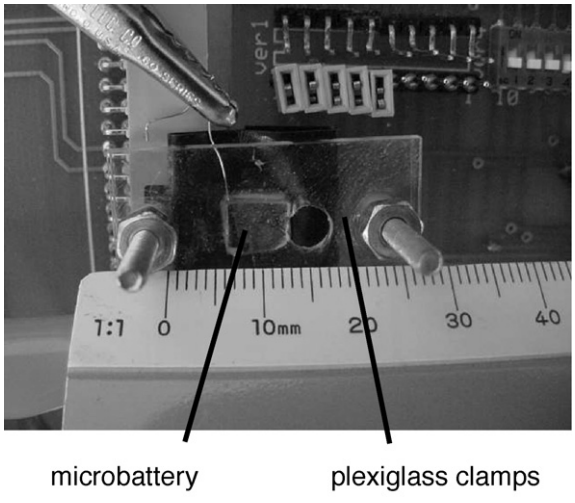

Fig. 3. Microbattery IOS-X-1, a cell with 5.24 mm^2 footprint to be integrated with the device microchip.

2.4.1. Description of stand-alone batteries

To map the influence of size over cell capacity and cycle life, we fabricated and tested five stand-alone cells using a Solartron® 1470E battery tester and a Maccor® 4000 series tester. The first three cells O(cm^2), which we will refer to as IOS-C-1, IOS-C-2 and IOS-C-3 throughout this work, had a footprint, respectively of 1.2, 1.0 and 1.0 cm^2, and the last two cells O(mm^2), which we will refer to as IOS-M-1, IOS-M-2, had a smaller footprint of 2 mm^2 (Table 4). Battery IOS-C-1 was designed to establish the capacity of thin-film Zn/AgO batteries and to evaluate their cycle life at constant discharge rate. Batteries IOS-C-2 and IOS-C-3 were constructed to estimate the influence of different discharge rates and to further evaluate cycle life. Batteries IOS-M-1 and IOS-M-2 were built to evaluate the ability of reducing battery size and to study the effects of size reduction. Battery IOS-C-1 was validated in 10 cycles of discharge and recharge at constant 250 μA (~1.4 C rate) current. A similar test, 10 cycles at constant 250 μA (~1.4 C rate) draw, was performed on battery IOS-C-3. Finally, battery IOS-M-1 was cycled five times at a constant 2.5 μA (~0.7 C rate) current. To estimate theoretical capacity as precisely as possible, batteries IOS-C-2 and IOS-M-2 were discharged at a very low rate in the Maccor® tester. IOS-C-2 discharged at a constant current of 2.5 μA (~C/70 rate); IOS-M-2 was discharged at a constant current of 25 nA (~C/150 rate).

2.5. Description of integrated battery

Battery IOS-X-1 was fabricated to investigate the effects of system integration, variable discharge rate and size reduction simultaneously. IOS-X-1 (Fig. 3) had an electrode surface area of 1.86 mm × 2.82 mm and an estimated cathode volume of 7.3×10^{-4} mm^3. The integrated device top view, microbattery IOS-X-1, DC/DC converter T68A-BE (voltage regulator) and microchip MOSIS T5AE-AA, is reported in Fig. 4. Initial microchip power was provided through an Agilent E3620A power supply (constant

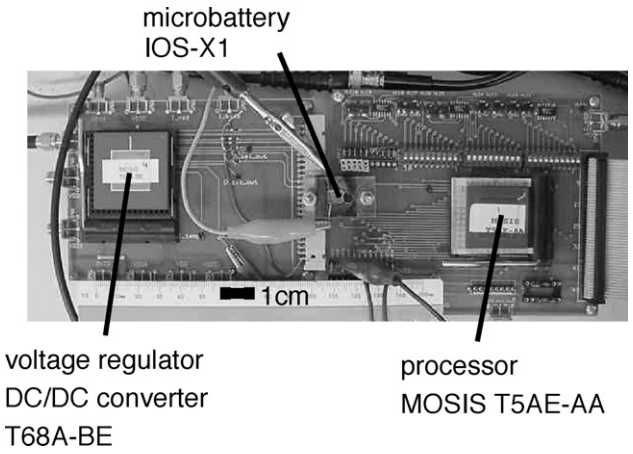

Fig. 4. Top view of IOS-X-1 with integrated system.

Table 4
Summary of characteristics and performance of all fabricated cells

Battery	Size (cm^2)	Cathode mass (g)	Theoretical capacity (μAh)	Current (μA)	1st cycle capacity (μAh)	% of theoretical capacity	Specific capacity ($\mu Ah\,cm^{-2}$)
IOS-C-1	1.2	1.8×10^{-4}	182	250 (~1.4 C)	100.00	55.0	83.3
IOS-C-2	1.0	1.8×10^{-4}		2.5 (~C/70)	11.25	6.2	11.3
IOS-C-3				250 (~1.4 C)	47.50	26.1	47.5
IOS-M-1	2.0×10^{-2}	3.6×10^{-6}	3.64	2.5 (~0.7 C)	2.75	75.5	137.5
IOS-M-2				0.025 (~C/150)	0.28	7.7	14.0
IOS-X-1	5.24×10^{-2}	7.7×10^{-6}	7.6	0.1–0.2 (~C/70-C/40)	1.10	14.5	21.0

0.62 V) and subsequently was switched to battery IOS-X-1. The current draw was variable, depending on the microchip operation. The battery voltage drop was recorded over time in a Keithley 6514 Pico-Voltmeter, while the current draw was monitored using a Keithley 6485 Pico-Ampmeter.

3. Results

3.1. POWER output results

For POWER [11] calculations all 194 primary batteries included in the present database version were considered. A Zn/AgO battery type Renata 317 [18] was the best candidate, due to its high nominal capacity (10.5 mAh), and low mass (0.18 g) and a volume (43.5 mm^3). The resulting projected lifetimes of all three approaches exceeded the targeted lifetime (≤2 years) by more than one order of magnitude. Among 61 secondary systems, a commercial Panasonic ML421S $LiMn_2O_4$ cell [19] and a research thin-film $LiCoO_2$ cell [25] met system requirements. The ML421S cell had a capacity of 2.3 mAh, with a mass of 0.11 g and a volume of 38 mm^3. The $LiCoO_2$ thin-film battery (from the reference) had a capacity of approximately 1 mAh, with a mass of 0.1 g and a volume of 1.5 mm^3. The electrochemistry Zn/AgO was considered to operate as a primary system, since secondary systems have been of very large scale [20], mainly for space and defense applications.

Secondary systems were also considered. Lifetimes of selected commercial $LiMn_2O_4$ cells exceeded 5 years (63.9-month long cycles) while research-grade $LiCoO_2$ battery projected lifetimes were approximately half of that (37-month long cycles). In estimation of secondary cell lifetimes, rechargeability was not considered, since the target lifetime for several candidates was already met when used as primary cells.

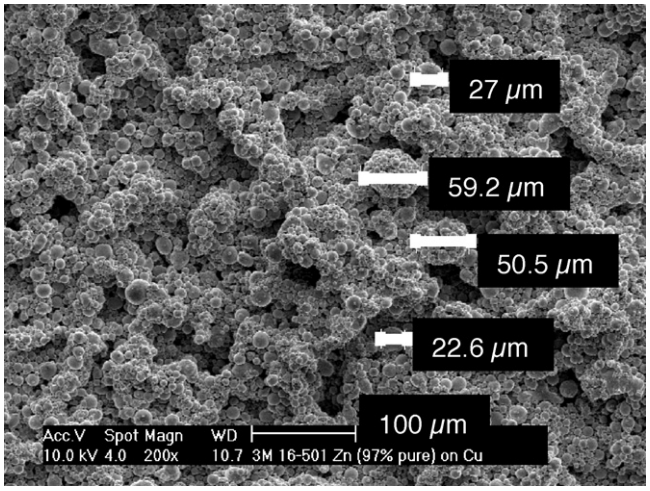

Fig. 5. SEM picture of Zn anode surface for IOS-C-1.

3.2. Fabricated novel cells

Sizes and masses of the cathodes (where the AgO was the electrode) for the fabricated cells are reported in Table 4. Cells final volumes (with package) ranged from 3.16 to 200 mm^3, while cell final masses varied from 0.15 to 2.78 g. The cathode mass varied from $\sim 3.6 \times 10^{-6}$ g (3.4×10^{-8} mol) to 1.8×10^{-4} g (1.7×10^{-6} mol). The anode mass was in excess with respect to the cathode by one order of magnitude, due to the different deposition technique that resulted thicker films (~10 μm), and the values varied from $\sim 9.1 \times 10^{-5}$ g (1.4×10^{-6} mol) to 10^{-2} g (1.5×10^{-4} mol). This design provided more than stoichiometric conditions; therefore the overall theoretical capacity of the Zn/Ag couple was limited by the cathode [21].

3.3. Theoretical calculations

Capacities of up to ~76% of theoretical values were achieved using the cathodes produced in our study (Table 4). The theoretical capacity, based on the cathode mass (1.7×10^{-6} mol), for IOS-1, IOS-2 and IOS-3 was 182 μAh. For the smaller cells IOS-M1 and IOS-M2 the theoretical capacity was ~3.64 μAh while for IOS-X1 ~7.61 μAh. To calculate the theoretical capacity, we assumed that all the silver present in the films was oxidized to AgO (oxidation number +2). Thus the electrochemical equivalent of cathode mass was calculated based on the following two simultaneous reactions in the cathode during discharge:

$$2AgO + H_2O + 2e^- \rightarrow Ag_2O + 2OH^- \qquad E^0 = +0.607\,V \qquad (1)$$

$$Ag_2O + H_2O + 2e^- \rightarrow 2Ag + 2OH^- \qquad E^0 = +0.342\,V \qquad (2)$$

For each mole of electrons (e^-) lost by the cathode in the discharge reaction, 26.8 Ah are produced theoretically; thus for each mole of AgO consumed at the cathode, four e^- mole are released through reactions (1) and (2), i.e. 107.2 Ah. Typically, the theoret-

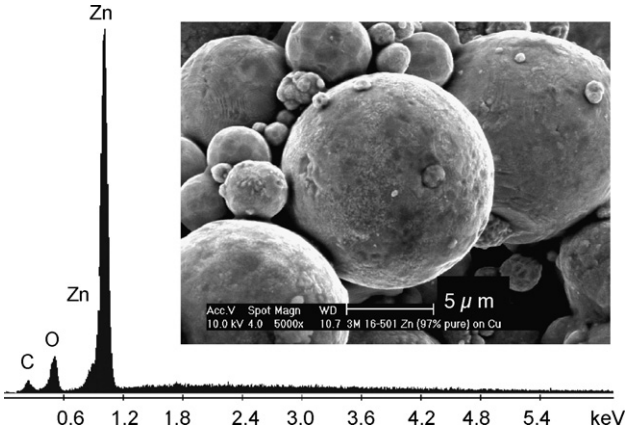

Fig. 6. Detail SEM picture of Zn anode particles and corresponding XEDS spectrum for IOS-C-1.

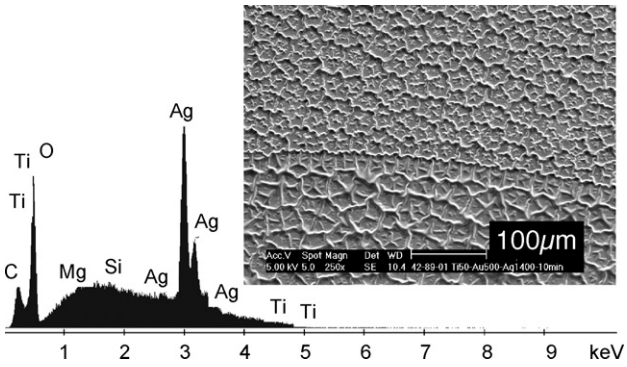

Fig. 7. SEM picture of AgO cathode surface and corresponding XEDS spectrum for IOS-C-1.

ical voltage resulting from the two reactions above is ≥1.7 V [21] with lower voltages indicating that only partial reactions are taking place.

3.4. Electrode microstructures

Electrode microstructure affects both theoretical capacity and conductivity of active materials [14,15]. Fig. 5 shows the surface of one of the anode samples. Deposited zinc (Zn) films were open porous structures, which preferred, for infiltration with liquid electrolyte. Fig. 6 is a detailed image of individual Zn particles, from the same sample, having diameters of 2–8 μm. The XEDS spectrum shows that zinc (Zn) was the main constituent, with some traces of carbon (C), presumably from the organic solvent of the aerosol spray. Fig. 7 illustrates the cathode surface and the XEDS spectrum, showing silver (Ag), oxygen (O), silicon (Si) and titanium (Ti) peaks. The XEDS spectrum only provides a qualitative measure of oxidation, since the intensity of each peak shows only the element's relative abundance in the area swept by the electron gun.

3.5. Stand alone batteries: discharge curves

Constant current discharge are shown in Fig. 8, for all O(cm^2) fabricated cells and Fig. 9, for all O(mm^2) fabricated cells. The initial output voltages of the cells were between 1.5 and 1.6 V. All tests were conducted with a cutoff voltage of 0.9 V upon discharge and 1.6 V upon recharge. Experimental capacity, extrapolated from the first discharge cycle for all batteries, ranged from 11.25 to 100 μAh for the bigger batteries O(cm^2), and from 0.25 to 2.75 μAh for the smaller ones O(mm^2). Battery IOS-C-1 and IOS-C-3 were cycled 10 times while battery IOS-M-1 was only cycled 5 times.

3.6. Integrated battery: discharge curves

The integrated battery IOS-X-1 discharge voltage and current versus time plots are reported in Fig. 10; overall achieved capacity under variable discharge conditions was 1.1 μAh. The first output voltage was ∼1.6 V, after the battery was sealed. The battery was able to power the chip for approximately 9 h before reaching 0.9 V cutoff. The current draw profile comprises three steps: 180 nA lasting approximately 1 h, followed by ∼130 nA during 3 h and ∼110 nA for 5 h.

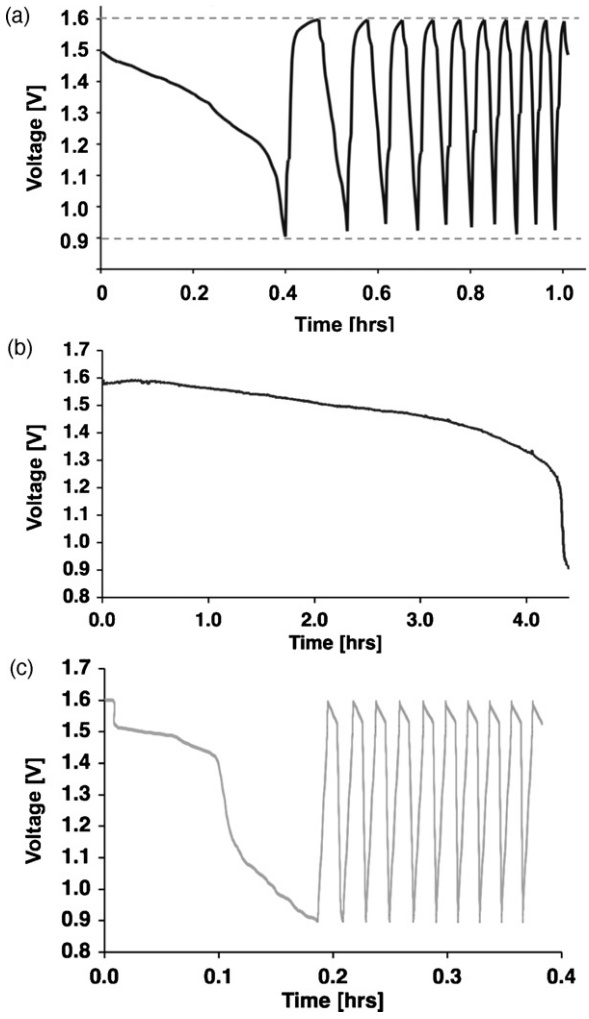

Fig. 8. Discharge profiles for O(cm^2) batteries: (a) IOS-C-1 250 μA (∼1.4 C), (b) IOS-C-2 2.5 μA (∼C/70), (c) IOS-C-3 250 μA (∼1.4 C).

4. Discussion

4.1. Comparison with state-of-the-art (SOA)

Our fabrication process is compatible with MEMS materials and allows battery electrodes to be deposited directly on chips or chip packages. Fabrication methods for other thin-film batteries are not generally compatible with MEMS production, because of high temperature (>800 °C [25]) and use of etchants and solvents [25,30]. Li thin-film batteries cost around $300/Wh [22] mainly related to the extensive use of the clean-room in the manufacturing process coupled with the numerous fabrication steps. Based on the raw material cost of Ag ($4.9/g) and Zn ($2.4/g), we estimated a materials cost of $8.3/Wh for our cells, though manufacturing costs are not yet easily estimated, to compare with present Li battery costs (Table 5).

The Zn/Ag nominal voltage (1.55 V) matches the present application requirements and is suitable for MEMS devices with similar bus voltages. Li-ion microbatteries [23–28,43–45] have been studied as thin-film cells for MEMS (Table 2) because their high nominal voltage (∼3.7 V) affords them a much higher specific energy than other electrochemistries, e.g. Ni/Zn (∼1.8 V) [29–31] or Ag/Zn (∼1.55 V). However the intrinsically high voltage can also necessitate use of operational amplifiers to power MEMS devices [7,8], because of low

Table 5
Comparison of fabricated prototypes to SOA and targets [9,18,25,27,49]

	SOA: Ag–Zn systems	SOA: Li systems	Present work: PVD	Targets
Thickness	2–5 mm	Limited to 0.5–5 μm (without package)-15 μm (with package) [2]	25 μm (without package)–1.7 mm (with package)	Depends on application
Footprint	≥10 mm^2	≥1 cm^2	0–1 mm^2	0–1 mm^2
Capacity	∼100 mAh cm^{-2}	∼0.1 mAh cm^{-2}	∼0.1 mAh cm^{-2}	20 mAh cm^{-2} [4]
Fabrication with MEMS	Add-ons	Incompatible	Compatible	Compatible
Stackable	NA	Capable, not demonstrated	Capable, not demonstrated	Necessary, given larger capacities
Bus voltage	Ag–Zn: ∼1.55 compatible with bus voltage, 1.5	Li: ∼3.5–4.5 V requires voltage regulation	Ag–Zn: ∼1.55 compatible with bus voltage, 1.5	Dropping

bus voltages in low-power systems; this, in turns, adds both mass and system complexity.

The batteries produced in our study had electrodes of thicknesses 140–170 nm, and overall thicknesses of ∼1.7 mm (including packaging); the surface areas were ≥2 mm^2 and similar to the device scale O(mm^2). Electrode thicknesses limit actual capacity in thin-film batteries, including those in the present work. Very small overall thicknesses, ∼15 μm (Li-ion) to ∼300 μm (Li-ion, Ni/Zn, Ag/Zn), have been achieved in several thin-film batteries (Table 2) with the smallest reported footprint being ∼1 cm^2. When we compare electrodes without packaging, the PVD electrodes (novel cells) were one-tenth the thickness of other thin-film electrodes, and comprised less than one-hundredth the surface area.

The impedance of silver–zinc cells is normally low, but can vary considerably with factors such as content of silver [21], discharge current, state-of-charge (SoC), cells aging, operational temperature, separator material and more importantly, cell size [32]. Differences among our results are likely to be a consequence of variation of impedance and degree of oxidation among the samples that we utilized to fabricate our batteries.

Direct on-chip fabrication is a key objective for size reduction and integration of the battery, and to realize a fully autonomous and implantable microsystem. Our approach enables a small overall volume (0.42 mm^3) of the IOS. The smallest of our prototypes had a volume of approximately 80% of a commercial system, neglecting nonfunctional packaging.

Capacities ranging from 6.2% to 75.5% of theoretical were achieved in our tested prototypes (Table 4). The higher content of Ag in cells with thicker cathodes (170 nm) resulted in lower internal resistance and better performance of the tested prototypes at higher rates. We believe that the extent of oxidation of the cathode films (amount of AgO/Ag_2O), resulting from different oxidation times (10–15 min) affected the capacity output; however a direct measurement of the AgO content in the cathodes was not performed. An initial voltage below 1.6 V indicates higher

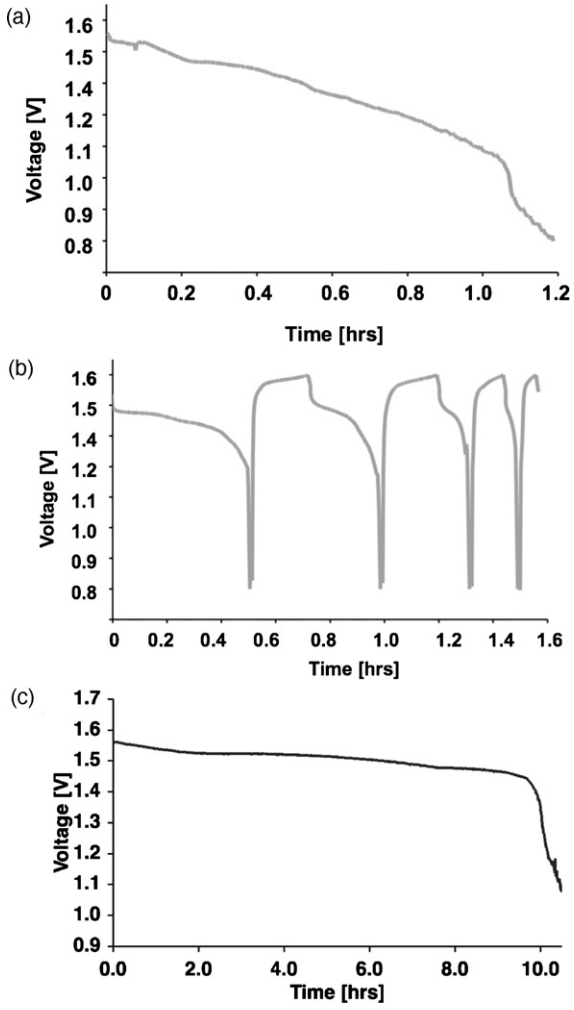

Fig. 9. Discharge profiles for O(mm^2) batteries: (a) IOS-M-1 1st cycle 2.5 μA (∼0.7 C), (b) IOS-M-1 2.5 μA (∼0.7 C), and (c) IOS-M-2 25 nA (∼C/150).

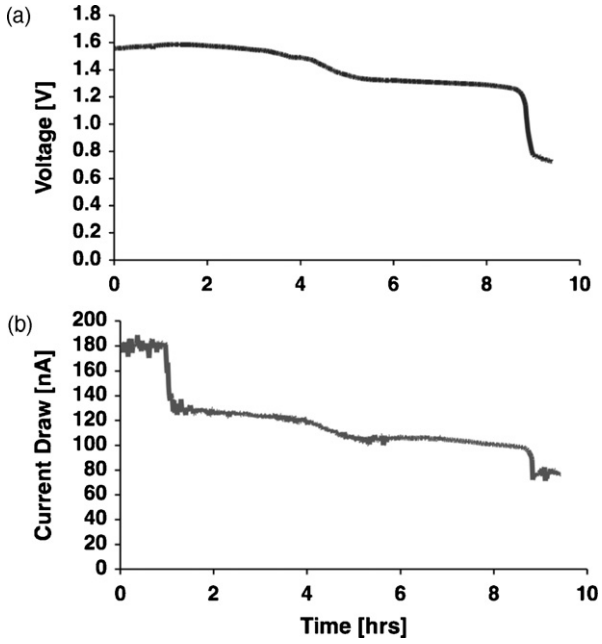

Fig. 10. Discharge profile for on-chip battery: (a) IOS-X-1 discharge voltage and (b) IOS-X-1 discharge current (∼100–200 nA).

content of monovalent silver oxide (+1) in the cathode. A change of slope in the discharge curve or the presence of an inflection point is related to the exhaustion of the first redox reaction at the cathode (divalent AgO) and onset of the second reaction (monovalent Ag_2O). The capacity of the integrated battery (IOS-X-1) was ~14% of theoretical. This value is considered separately, since the test was conducted at a variable discharge rate between 100 and 200 nA. These results are consistent with other reports, wherein variable discharge rates have been shown to affect the battery performance by more than 50% [33]. Compared to commercial Zn/AgO systems (e.g. the ones reported in Table 3) that provide as low as 2–3% of theoretical capacity, the present batteries offered an order of magnitude improvement in actual versus theoretical capacity, supporting our underlying hypothesis.

The batteries deposited in our study achieved a specific capacity $\leq$138 $\mu Ah\,cm^{-2}$ and were comparable to the thin-film batteries reported in the literature, whose specific capacities ranged from 20 to 300 $\mu Ah\,cm^{-2}$. Wireless sensor networks based on MEMS technology require higher capacities, up to 20 $mAh\,cm^{-2}$ [9]. Higher specific capacities may be achieved in the future by designing batteries with 3D architectures

4.2. Limitations of present work

The differences between theoretical and experimental capacities across fabricated batteries are likely to be the result of a combination of several factors.

Even though recharging is not required for the present application as the batteries could meet the target lifetime when used as primary cells, it is important to be able to recharge the device if longer treatment periods are required. The cycle life of the present prototypes needs improvement if the rechargeability of the device becomes a goal. This could be achieved by employing special separators or introducing additives that limit dendrite growth, increase conductivity and accelerate diffusion processes. Loss of electrolyte also affected battery performance and rechargeability. Upon recharge, lower rates of discharge resulted in lower capacity recovery, this is unusual and partly due to package seal and evaporation of electrolyte. We believe that, as the time of discharge is longer for these cells, electrolyte evaporation, electrode dissolution and dendrite formation phenomena may be more important and limit the recovered capacity. Several batteries had failures in their hermetic seals, resulting in electrolyte leakage and evaporation; this prevented recharge. Due to the implantable nature of the sensor, this is a particularly critical challenge to address because it directly affects safety and lifetime of the device. Parylene-C [34] is a suitable alternative to the present package as can be deposited, in the gas phase, as a biocompatible and stress-resistant film.

Self-discharge, in cells having millimeter and sub-millimeter size, is a factor that has a relevant influence on battery lifetime [35], in the present application this could prevent achieving the 2 years lifetime required shortening the device lifetime. Long-term testing of the battery needs to be performed in order to establish the battery shelf life. Injection of electrolyte and activation of the cell as needed could prevent self-discharge. Another measure that could be implemented, after the battery has been activated, is the design of hybrid systems including capacitors or energy scavenging devices [36] that could prevent discharge and enhance lifetime of the battery and of the device.

Finally, the extent of the oxidation, and therefore the content of active AgO/Ag_2O material in the cathode, directly affects the capacity of the cell and the achieved voltage. The cathode film (limiting electrode) could be made of AgO (oxidation number +2), Ag_2O (oxidation number +1) or a combination of the two, while non-oxidized parts of the cathode would still contain pure Ag. In our theoretical capacity calculations, we assumed a cathode made 100% of AgO with a theoretical voltage higher than 1.7 V. The pure silver (Ag) in the cathode (nonoxidized, or that is produced during the chemical reaction upon recharge), increases the cathode conductivity keeping the internal resistance of the cell low [21].

5. Conclusions

Systems like the WIMS-IOS, requiring variable power profiles over time (e.g. pulses, spikes or steady plateaux) or comprising combinations of subcomponents, provide an opportunity for hybridization of power supplies, comprising more than one cell and/or electrochemistry. Modeling the duty cycle of the WIMS-IOS, an intrinsically low power system (42 pW $cycle^{-1}$), we were able to identify and design a suitable power source [11,12]. The present application is both an implantable device and a low-power MEMS (1.6 V maximum), thus Zn/AgO represents a natural choice over Li (nominally 3.7 V). Regulation of 3.7 V (optimal for high power applications) to lower levels requires energy dissipation (waste), usage of electronics circuitry, cells in special configurations (parallel or in series with resistors) and additional control units.

The capacity and lifetime of Zn/AgO fabricated microbatteries ($\leq$76% of theoretical) was superior to available commercial systems (as low as 2–3% of theoretical). Five stand-alone cells were created and successfully discharged: three O(cm^2) microbatteries (IOS-C-1, IOS-C-2 and IOS-C-3) and two O(mm^2) microbatteries (IOS-M-1, IOS-M-2). Cells were fabricated with footprints of 1.2 and 1.0 cm^2 for the larger cells, and 2.0 mm^2 the smaller cells (Table 4). The highest experimental capacity among the larger cells was 100 μAh, achieved by IOS-C-1 at 250 μA (1.4 C) discharge. Among O(mm^2) cells (Table 4), IOS-M-1 achieved the highest capacity (2.75 μAh, ~76% of theoretical) at 2.5 μA discharge (0.7 C rate).

Our microbatteries are projected to meet the application lifetime requirements ($\leq$2 years). Based on the experimental capacity of battery IOS-M1 (2.75 μAh), the energy content of this cell is ~4.26 μWh under a nominal voltage of 1.5 V. Without losses, such battery could operate the device for ~101,428 cycles of 10 min, i.e. for ~16,904 h or ~1.93 years.

Future work will focus on improving manufacturing, and more detailed interrogation of the effects of microstructure on performance. This work will be focused on enabling ever smaller, and more efficient, power supplies for autonomous MEMS. Self-discharge evaluation and long term testing are necessary due to the implantable nature of this application. Testing at 37 °C to replicate body temperature, accurate evaluation of the reaction byproducts, oxygen formation during recharge, are necessary to estimate the long term effects of implantation on the power source. Additional optimization criteria will results from this analysis, and it is anticipated that additional engineering approaches to design and optimization [37] will be required.

Acknowledgements

We acknowledge Mr. Scott Hanson for providing information about the power consumption of the intraocular sensor microchip. Dr. Sigrun Karlsdottir for training using the SEM microscope. Prof. Max Shtein for providing the Ångstrom Engineering PVD machine and Mr. Brendan O'Connor and Mr. Andrea Bianchini for providing assistance in preparing the samples. Sponsorship of this effort was primarily from the Engineering Research Centers program of the National Science Foundation under NSF Award Number EEC-9986866; support for some of the facilities used in this project was provided by the Assistant Secretary for Energy Efficiency and Renewable Energy, Office of FreedomCAR and Vehicle Technologies

of the U.S. Department of Energy under contract No. DE-AC02-05CH11231, subcontract No. 6720903.

References

[1] D.F. Lemmerhirt, K.D. Wise, Proceedings of the IEEE 94 (6) (2006) 1138–1159.
[2] H. Sato,C.W. Berry, B.E. Casey, G. Lavella, Y. Yao, J.M. VandenBrooks, M.M. Maharbiz, A Cyborg beetle: insect flight control through an implantable, tetherless microsystem, 21st IEEE International Conference on Micro Electro Mechanical System, 13–17 January 2008, 164–167.
[3] P. Mohseni, K. Najafi, S.J. Eliades, X.Q. Wang, IEEE Transactions on Neural Systems and Rehabilitation Engineering 13 (3) (2005) 263–271.
[4] A. Nieder, Journal of Neuroscience Methods 101 (2) (2000) 157–164.
[5] E.A. Johannessen, L. Wang, L. Cui, T.B. Tang, M. Ahmadian, A. Astaras, S.W.J. Reid, A.F. Murray, B.W. Flynn, S.P. Beaumont, D.R.S. Cumming, J.M. Cooper, IEEE Transactions on Biomedical Engineering 51 (3) (2004) 525–535.
[6] I. Obeid, M.A.L. Nicolelis, P.D. Wolf, Journal of Neuroscience Methods 133 (1/2) (2004) 33–38.
[7] M. Seok, S. Hanson, Y.-S. Lin, Z. Foo, D. Kim, Y. Lee, N. Liu, D.M. Sylvester, D. Blaauw, The Phoenix processor: a 30 pW platform for sensor applications, IEEE International VLSI Circuits Conference, 18–20 June 2008, 188–189.
[8] Y.-S. Lin, S. Hanson, F. Albano, C. Tokunaga, R.-U. Haque, K.D. Wise, A.M. Sastry, D. Blaauw, D.M. Sylvester, Low-voltage circuit design for widespread sensing applications, IEEE International Symposium on Circuits and Systems, ISCAS 2008, 18–21 May 2008, 2558–2561.
[9] J.W. Long, B. Dunn, D.R. Rolison, H.S. White, Chemical Reviews 104 (10) (2004) 4463–4492.
[10] F. Albano, A.M. Sastry, Provisional Patent Application No.: 60/938232, Micromachined Deposited Battery, Provisional Application Date, 16.05.07.
[11] K.A. Cook, F. Albano, P.E. Nevius, A.M. Sastry, Journal Of Power Sources 159 (1) (2006) 758–780.
[12] K.A. Cook, A.M. Sastry, Journal of Power Sources 140 (1) (2005) 181–202.
[13] F. Albano, M.D. Chung, D. Blaauw, D.M. Sylvester, K.D. Wise, A.M. Sastry, Journal of Power Sources 170 (1) (2007) 216–224.
[14] C.-W. Wang, A.M. Sastry, K.A. Striebel, K. Zaghib, Journal of the Electrochemical Society 152 (5) (2005) A1001–A1010.
[15] C.-W. Wang, Y.-B. Yi, A.M. Sastry, J. Shim, K.A. Striebel, Journal of the Electrochemical Society 151 (9) (2004) 1489–1498.
[16] http://www.angstromengineering.com/evolution-vacuum-technology.htm, accessed 22.03.07.
[17] http://products3.3m.com/catalog/us/en001/utilities_telecom/electrical_contractors/node_GSGXVSC57Rgs/root_GST1T4S9TCgv/vroot_GSBCDFDZ1Zge/bgel_GSRYBL3GPVbl/gvel_Q2V48VRQDBgl/command_AbcPageHandler/theme_us_electricalcontractors_3_0, accessed 27.03.07.
[18] http://www.renata.com/pdf/watch/DB317.pdf, accessed 23.01.08.
[19] http://products.panasonic-industrial.com/datasheets/en/ML414S.pdf, accessed 25.11.07.
[20] http://www.yardney.com, accessed 06.01.08.
[21] D. Linden, T.B. Reddy, Handbook of Batteries, McGraw-Hill, New York, New York, 2002.
[22] http://www.infinitepowersolutions.com, accessed 02.06.07.
[23] B. Bates, N.J. Dudney, B. Neudecker, A. Ueda, C.D. Evans, Solid State Ionics 135 (1–4) (2000) 33.
[24] J.B. Bates, N.J. Dudney, B.J. Neudecker, F.X. Hart, H.P. Jun, S.A. Hackney, Journal of the Electrochemical Society 147 (1) (2000) 59.
[25] B.J. Neudecker, N.J. Dudney, J.B. Bates, Journal of the Electrochemical Society 147 (2) (2000) 517.
[26] B.J. Neudecker, R.A. Zuhr, J.B. Bates, Journal of Power Sources 82 (1999) 27.
[27] N.J. Dudney, B.J. Neudecker, Current Opinion in Solid State and Materials Science 4 (5) (1999) 479.
[28] J.B. Bates, N.J. Dudney, D.C. Lubben, G.R. Gruzalski, B.S. Kwak, X.H. Yu, R.A. Zuhr, Journal of Power Sources 54 (1) (1995) 58–62.
[29] P.H. Humble, J.N. Harb, R. LaFollette, Journal of the Electrochemical Society 148 (12) (2001) A1357.
[30] J.N. Harb, R.M. LaFollette, R.H. Selfridge, L.L. Howell, Journal of Power Sources 104 (1) (2002) 46.
[31] R.M. LaFollette, J.N. Harb, P. Humble, Sixteenth Annual Battery Conference on Applications and Advances, 2001, p. 349.
[32] B. Hariprakash, S.K. Martha, A.K. Shukla, Journal of Power Sources 117 (1/2) (2003) 242–248.
[33] M. Venkatraman, J.W. Van Zee, Journal of Power Sources 166 (2) (2007) 537–548.
[34] M. Tunc, X.H. Cheng, B.D. Ratner, E. Meng, M. Humayun, Retina—The Journal of Retinal and Vitreous Diseases 27 (7) (2007) 938–942.
[35] K.B. Lee, L.W. Lin, Journal of Microelectromechanical Systems 12 (6) (2003) 840–847.
[36] S. Roundy, D. Steingart, L. Frechette, P. Wright, J. Rabaey, Wireless Sensor Networks Proceedings 2920 (2004) 1–17.
[37] X. Zhang, A.M. Sastry, W. Shyy, Intercalation-induced stress and heat generation inside lithium-ion battery cathode particles, Journal of the Electrochemical Society 154 (10) (2007) A910–A916.
[38] http://www.wimserc.org, accessed July 2005, intraocular testbed (conceptual device).
[39] A.M. Cardenas-Valencia, J. Dlutowski, S. Knighton, C.J. Biver, J. Bumgarner, L. Langebrake, Sensors and Actuators B: Chemical 122 (1) (2007) 328–336.
[40] C. Navone, J.P. Pereira-Ramos, R. Baddour-Hadjean, R. Salot, Journal of the Electrochemical Society 153 (12) (2006) A2287–A2293.
[41] K. Kushida, K. Kuriyama, T. Nozaki, Applied Physics Letters 81 (26) (2002) 5066–5068.
[42] S.D. Jones, J.R. Akridge, Journal of Power Sources 54 (1) (1995) 63–67.
[43] K.A. Striebel, C.Z. Deng, S.J. Wen, E.J. Cairns, Journal of the Electrochemical Society 143 (1996) 1821–1827.
[44] A. Rougier, K.A. Striebel, S.J. Wen, T.J. Richardson, R.P. Reade, E.J. Cairns, Applied Surface Science 134 (6) (1998) 107–115.
[45] K.A. Striebel, A. Rougier, C.R. Horne, R.P. Reade, E.J. Cairns, Journal of the Electrochemical Society 146 (12) (1999) 4339–4347.
[46] S.-W. Song, R.P. Reade, E.J. Cairns, J.T. Vaughey, M.M. Thackeray, K.A. Striebel, Journal of the Electrochemical Society 151 (7) (2004) A1012–A1019.
[47] Small commercial cells, designed for low-drain applications (watch batteries, etc.) have much lower practical power densities because the hardware and other inert components (coin cell cases, etc.) take up a much larger fraction of the total weight compared to larger batteries designed for high power.
[48] A.P. Karpinski, S.J. Russell, J.R. Serenyi, J.P. Murphy, Journal of Power Sources 91 (2000) 77–82.
[49] www.minatec.com/minatec2003/act_pdf/4_THURSDAY_ROUX.pdf, accessed 24.01.08.